Supercritical CO_2 Activation Enables an Exceptional Methanol Synthesis Activity Over the Industrial $Cu/ZnO/Al_2O_3$ Catalyst

Yannan Zhou, Jingyun Jiang, Yushun Wang, Ruijie Liu, Shouren Zhang,* and Jianfang Wang**

The ternary $Cu/ZnO/Al_2O_3$ catalyst is widely used in the industry for renewable methanol synthesis. The tenuous trade-off between the strong metal–support interaction (SMSI)-induced $Cu–ZnO_x$ interface and the accessible Cu surface strongly affects the activity of the final catalyst. Successes in the control of oxide migration on adsorbate-induced SMSI catalysts have motivated this to develop a supercritical CO_2 activation strategy to synchronously perfect the $Cu^0–O–Zn^{\delta+}$ interface and $Cu^0–Cu^+$ surface sites through the manipulation of the adsorbate diffusion kinetics, which involves $^*OC_2H_5$ and "side-on" fixed CO_2 species. This findings illustrate that the adsorbate on ZnO_x can facilitate its secondary uniform nucleation and induce a $Zn_xAl_2O_y$ spinel phase and that CO_2 adsorption on metallic Cu^0 produces an activated Cu_xO amorphous shell. Such a structural evolution unlocks a dual-response pathway in methanol synthesis, thus enabling $Cu/ZnO/Al_2O_3$ with a twofold increase in catalytic activity. This atomic-level design of active sites and understanding of supercritical CO_2-induced structural evolution will guide the future development of high-performance supported metal catalysts.

1. Introduction

Methanol synthesis from captured off-gas CO_2 and non-fossil hydrogen through a one-step catalytic process is the heart of the Carbon Neutral Methanol Economy.[1] The leading industrial methanol catalyst, ternary $Cu/ZnO/Al_2O_3$ with Cu,Zn-containing nanoparticles (5–10 nm in size, molar ratio Cu:Zn = 7:3) supported on the structural promoter Al_2O_3,[2] has been producing ≈110000 tons of renewable CH_3OH and thus recycling ≈150000 tons of CO_2 per year.[3] Although this catalytic process has been studied for centuries, the synergistic effect of Cu and ZnO and the dynamic nature of Zn species are still under high debate.[4] Studies have shown that the active $Cu^0–O–Zn^{\delta+}$ interface created by the migration of reducible ZnO_x over the metallic Cu nanoparticle under strongly reducing reaction conditions,[5] the so-called strong metal support interaction (SMSI), and the accessible Cu surface, are essential to the catalytic performance. This, therefore, highlights the significance of a highly defective or porous oxide overlayer in the SMSI effect. This configuration, where the oxide partially covers the metal nanoparticle, allows reactants to interact with most exposed metal sites.[6]

Nevertheless, the uncontrollable kinetics of the SMSI are insufficient to create an optimal SMSI encapsulation state.[7] The

---

Y. Zhou, R. Liu, S. Zhang
Henan Provincial Key Laboratory of Nanocomposites and Applications
Institute of Nanostructured Functional Materials
Huanghe Science and Technology College
Zhengzhou, Henan 450006, China
E-mail: shourenzhang@infm.hhstu.edu.cn

J. Wang
Department of Physics
The Chinese University of Hong Kong
Shatin, Hong Kong SAR 999077, China
E-mail: jfwang@phy.cuhk.edu.hk

J. Jiang
College of Materials Science and Engineering
Zhengzhou University
Zhengzhou, Henan 450052, China
E-mail: jiangjingyun@zzu.edu.cn

Y. Wang
School of Chemistry and Chemical Engineering
Henan University of Science and Technology
Luoyang, Henan 471023, China

The ORCID identification number(s) for the author(s) of this article can be found under https://doi.org/10.1002/advs.202500118

DOI: 10.1002/advs.202500118

ZnO_x overlayer might cover all metal sites or affect only a minor portion of the interfacial sites. In addition, the dynamic nature of the ZnO_x component at elevated pressures and temperatures could lead to the excessive growth and partial crystallization of ZnO_x.[8] This will potentially reduce the density of the interfacial active sites or cause catalyst deactivation.[9] Recent progress has demonstrated that hydrocarbon species derived from CO_2 gas, and reductive alcohols, such as methanol, can lead to adsorbate-induced SMSI (A-SMSI) on the catalyst under mild conditions. The resultant encapsulating overlayer is usually permeable to reactant gases.[10] One important key to such an A-SMSI phenomenon is the control of the adhesive properties of alcohols, which have been observed to correlate with the migration of oxide species.[11] Highly adhesive EtOH tends to be physisorbed on the surface of the defective oxide, leading to the partial or complete poisoning of active sites and preventing the migration of oxide species. These investigations on the A-SMSI effect and how it affects the migration ability of oxide species have intrigued us and led us to develop an activation strategy to optimize the SMSI-induced catalyst structure through the control of the adsorbate kinetics.

Herein we demonstrate that the adsorbate diffusion kinetics on the $Cu/ZnO/Al_2O_3$ catalyst can be manipulated in a density-fluctuating supercritical (SC) CO_2–EtOH medium at a low temperature of 40 °C. Multiple in situ spectroscopy and microscopy show that controllable adsorbate diffusion results in the synchronous perfecting of SMSI-induced Cu^0–O–$Zn^{\delta+}$ interface and exposed Cu^0–Cu^+ surface active sites. Specifically, adsorbed $^*OC_2H_5$ and CO_2 species on the support guide the secondary nucleation of small-sized ZnO on the Cu surface and the formation of a new $Zn_xAl_2O_y$ phase, while CO_2 adsorption on metallic Cu^0 yields a large accessible activated Cu_xO surface area. We reveal that such an activation treatment renders the $Cu/ZnO/Al_2O_3$ catalyst resistant to the Cu sintering and ZnO_x recrystallization under working conditions. Moreover, it facilitates a dual-response pathway in the methanol synthesis from CO_2 hydrogenation, involving (i) formate and (ii) reverse water gas shift (RWGS) + CO hydrogenation mechanisms, thus improving the activity, selectivity, and stability. Under optimal conditions, the 12 MPa (4 h) catalyst exhibits the highest mass-specific methanol formation rate of 259.09 g kg_{cat}^{-1} h^{-1} at 210 °C, which is 2.1 times higher than that of the industrial catalyst (125.87 g kg_{cat}^{-1} h^{-1}). Our results show that controlling the kinetics of adsorbate diffusion represents a powerful support effect that enables the rational manipulation of the catalyst structure.

2. Results and Discussion

2.1. Catalytic Performance

The reduced industrial $CuO/ZnO/Al_2O_3$ catalyst, hereafter referred to as CZA_r (see Experimental Section in the Supporting Information for the details), was subjected to different activation treatments in the SC CO_2–EtOH system and subsequently evaluated for the CO_2 hydrogenation reaction in a Harrick reactor under pressurized (21 bar) and atmospheric pressure conditions (Figure S1, Supporting Information). The activated catalysts are denoted as *X* MPa (*Y* h), with *X* and *Y* being the activation pressure and time in the SC CO_2–EtOH system, respectively. **Figure 1**, Figures S2 and S3 (Supporting Information) display the steady-state reactivity data of our catalysts at different temperatures. The catalysts were pre-treated in situ with H_2 before the methanol synthesis reaction. To differentiate the hydrogen reduction of the catalyst during the preparation process, the in situ H_2 treatment is designated as H_2 treatment②. CO was the only detected gaseous byproduct for our catalysts.

Significant enhancement in MeOH production was observed over the activated samples at atmospheric pressure (Figure 1A). The MeOH space time yield (STY) maximized at 14.18 g kg_{cat}^{-1} h^{-1} over the 12 MPa (4 h) sample and decreased to 8.96 g kg_{cat}^{-1} h^{-1} when the SC CO_2 pressure was raised to 16 MPa. In addition, the methanol selectivity slightly increased from 20% to 32% after activation. The activities of the catalysts were further tested at 21 bar and temperatures from 170 to 250 °C (Figure 1B and Figure S2, Supporting Information). The MeOH STY increased from 55.96 to 629.28 g kg_{cat}^{-1} h^{-1} as the temperature was raised, delivering a superior MeOH yield (259.09 g kg_{cat}^{-1} h^{-1} at 210 °C) in comparison with CZA_r (125.87 g kg_{cat}^{-1} h^{-1} at 210 °C) and other reported state-of-the-art catalysts (Figure 1C and Table S1, Supporting Information). Notably, the most active catalyst (12 MPa (4 h)) in our study exhibited a much higher selectivity (89%) toward MeOH at 210 °C, with a high CO_2 conversion of 14.75%. Moreover, changing the reducing gas conditions (250 °C, 2 h) had a negligible effect on the activity of the catalyst (Figure S2, Supporting Information), while the pre-activation time of SC CO_2 was directly related to the activity of the catalyst. The temporal evolution of the MeOH production of the 12 MPa (4 h) sample at higher temperatures (210 and 250 °C) for 30 h is displayed in Figure 1D and Figure S3 (Supporting Information), respectively, featuring a superior stability. In addition, the fresh 12 MPa (4 h) sample without H_2 treatment② also showed a higher MeOH production than the CZA_r catalyst, even under atmospheric pressure (Figure S4, Supporting Information).

2.2. Catalyst Structural Evolution

To find out the underlying structural explanation for the observed trend, we performed X-ray diffraction (XRD) and quasi in situ X-ray photoelectron spectroscopy (XPS) measurements on the fresh and activated catalysts. All catalysts show comparable specific surface areas (55 m^2 g^{-1}), pore characteristics (pore volume, 0.25–0.28 cm^3 g^{-1}; average pore diameter, 19.28–23.43 nm), Cu and Zn contents, indicating overall structural robustness (Table S2 and Figure S5, Supporting Information). A significant decrease in the diffraction peak intensity for the SC CO_2-activated samples reveals an increase in amorphization (**Figure 2A**).[12] Additionally, the average crystallite sizes of the metallic Cu^0 nanoparticles, derived from the Cu (111) peak, were found to be 9.3 (CZA_r), 8.7 (12 MPa), and 9.8 (16 MPa) nm, respectively, indicating pressure-dependent grain sizes. The reduced grain size is related to the increased number of the Cu^0–O–$Zn^{\delta+}$ interface active sites, as confirmed by N_2O reactive frontal chromatography (N_2O-RFC) measurements.[13]

Notably, a new peak at 31.2° appears on the 12 MPa (4 h) sample. It is associated with the (220) plane of $ZnAl_2O_4$. The formation of Zn,Al-spinel in the CZA_r catalysts under reaction conditions usually involves the crystallization of amorphous Al-oxide

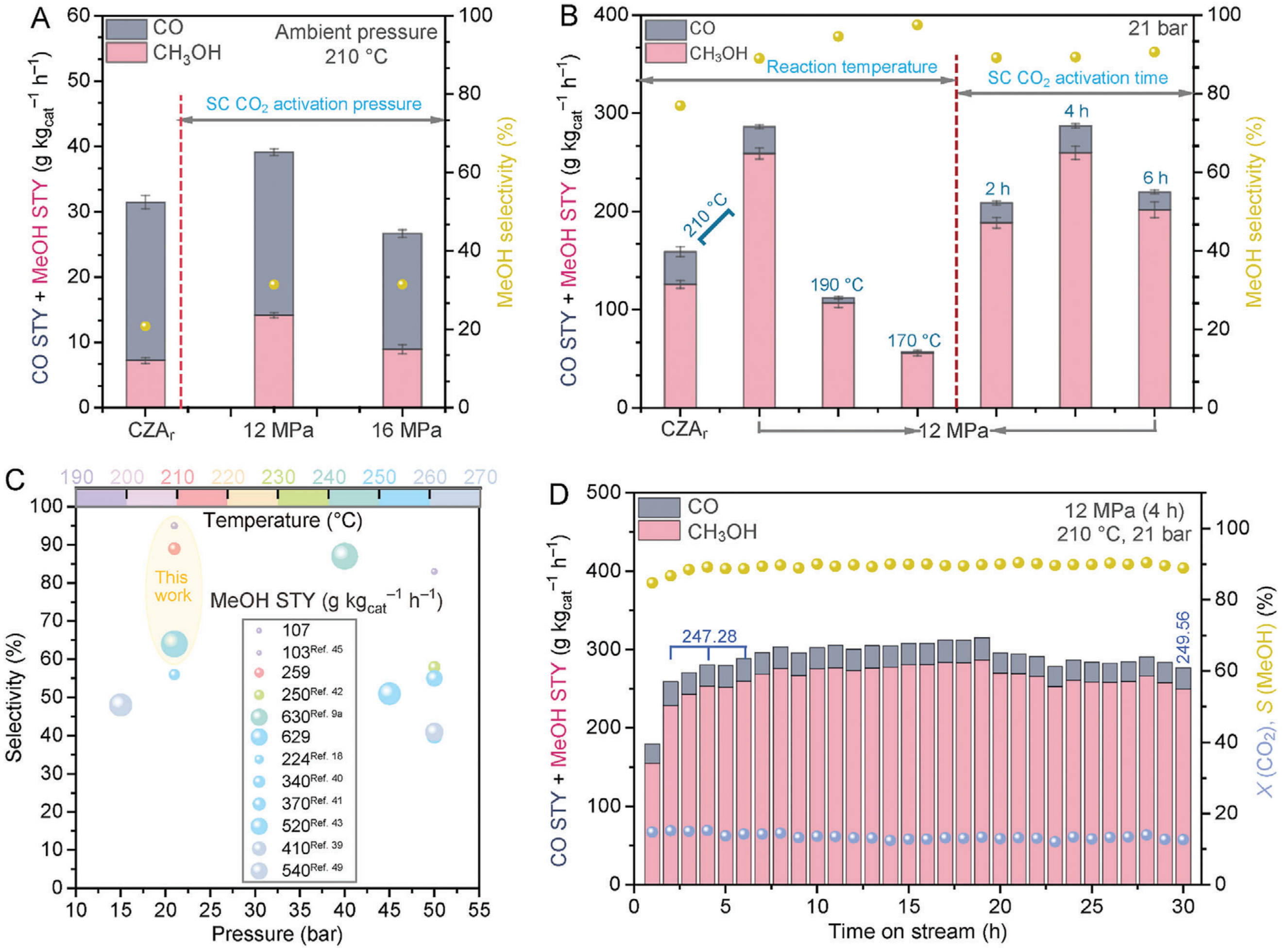

Figure 1. Performances of the different catalysts in CO_2 hydrogenation to methanol. A) MeOH selectivities and STYs of the differently activated catalysts for the reactions at 210 °C and atmospheric pressure. B) MeOH selectivities and STYs for the reactions at 170–210 °C and 21 bar. In all cases, results are expressed as mean ± SEM ($n = 3$), and significance was defined as $p < 0.05$. C) Performance comparison between the 12 MPa (4 h) catalyst and other reported Cu-based catalysts for methanol production from CO_2 hydrogenation. D) Stability test of the 12 MPa (4 h) catalyst over 30 h. The catalyst was pre-treated in situ with H_2 at 350 °C for 1 h. Reaction conditions: molar ratio CO_2:H_2 = 1:3, 20 mg catalyst, flow rate 20 mL min^{-1}. The reaction activity tests were conducted in a Harrick reactor.

species and consumption of crystalline ZnO, which would lead to catalyst deactivation.[14] In contrast, no diffraction peaks of Al-oxide species were observed on our samples, and the crystallinity of ZnO decreased after activation, suggesting a different formation mechanism of the spinel phase in the SC CO_2–EtOH system. Note that the formation of $Zn_xAl_2O_y$ can hinder the reduction of $Zn^{\delta+}$ species and the sintering of Cu nanoparticles under long-term reaction, thereby enhancing the stability of the activated catalysts (Figure 2B and Figure S6, Supporting Information).[15] The decrease in the intensity of the diffraction peak for $Zn_xAl_2O_y$ is probably caused by reaction-driven surface reconstruction.[16] The XPS results of Zn $2p_{3/2}$ for the fresh and spent catalysts at 210 °C and 21 bar further reveal changes in the Zn coordination environment (Figure S7, Supporting Information).[17]

Quasi in situ XPS analysis provided deep insights into the near-surface structure of the tested catalysts. The atomic ratio of Cu to Zn follows the order of 12 MPa (4 h) (0.83) > 16 MPa (4 h) (0.77) > CZA_r (0.75), indicating that the coverage of ZnO_x on the Cu surface induced by SMSI is reduced after activation. This observation indicates that the optimal catalyst activity is not dominated by the Cu–ZnO_x interfaces, which are recognized as the sole active sites for methanol synthesis.[18] The Cu and Zn LMM Auger spectra (Figure 2C,E) show that the surface proportion of Cu^+ species increases after further treatment in the SC CO_2–EtOH system, whereas with a lower proportion of $Zn^{\delta+}$ species.[13,19] Upon further exposure to H_2 at 350 °C, a complete reduction of Cu occurred in CZA_r, as evidenced by the disappearance of the Cu^+ signal. Nevertheless, the Auger parameter of Cu for the activated catalysts differs from that of CZA_r, evidencing a mixture of Cu^0 and Cu^+ (Figure S8, Supporting Information). More intriguingly, the amounts of $Zn^{\delta+}$ in the activated catalysts increase significantly. Under reaction conditions at 210 °C (21 bar or atmospheric pressure), a further decrease in the atomic percentages of Cu^+ and $Zn^{\delta+}$ was observed on the CZA_r catalyst (Figure 2D,F and Figure S9, Supporting Information). However, the reaction mixture only slightly reduces the amount of $Zn^{\delta+}$ in

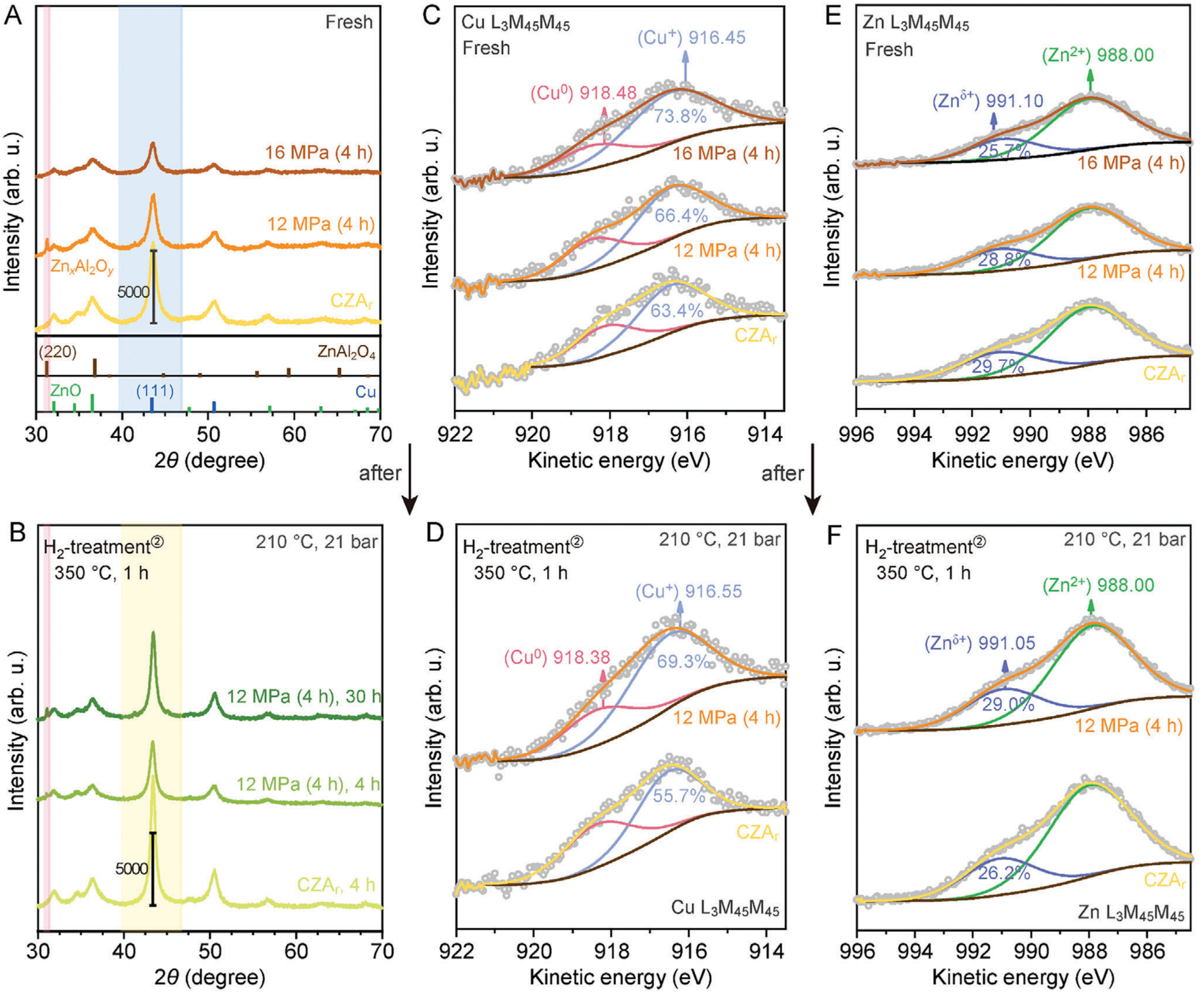

Figure 2. Structures of the fresh and spent catalysts at 210 °C and 21 bar. A,B) XRD patterns. C–F) Quasi in situ XPS Auger spectra of Cu LMM (C,D) and Zn LMM (E,F).

the activated samples, indicating a higher stability. The increased amount of Cu^+ might result from the reformation of a slight overlayer.

High-angle annular dark-field scanning transmission electron microscopy (HAADF STEM) imaging and energy-dispersive X-ray (EDX) mapping confirmed structural changes after the SC CO_2 treatment. The HRTEM images show the apparent amorphization of Cu nanoparticles for the activated samples (Figures S10 and S11, Supporting Information). SC CO_2-induced amorphization has been demonstrated before, where metallic Cu° can be oxidized to amorphous Cu_xO species with a high selectivity for C2+ products.[20] Detailed analysis of the lattice spacing distribution suggested that ZnO overlayer on Cu nanoparticles with an uncontrollable SMSI phenomenon in the CZA_r catalyst, i.e., fully covered Cu nanoparticles, coexist with partially covered and partially uncovered ones (**Figures** 3A and S12, Supporting Information). The EDX line scans across a particle in CZA_r show a Cu:Zn atomic ratio of 3.5 in the near-surface region (Figure 3B), which is consistent with previously reported results. The Cu:Zn atomic ratio at the surface of the catalyst decreased after reducing H_2 treatment.[21] However, activating the catalyst with the SC CO_2–EtOH system initiated clear reconstruction at the Cu–ZnO_x interface. The ZnO overlayer vanished in 12 MPa (4 h) but became richer in the 16 MPa (4 h) sample (Figure 3C–F).

The retraction of overgrown ZnO on the surface of the 12 MPa (4 h) sample was also evidenced by an increased Cu:Zn atomic ratio of 4.61. In the high-performance catalyst studied in our work, ZnO with a small particle size (<5 nm) is uniformly distributed around the Cu particles, contributing to the exposure of a large Cu surface area of up to ≈87.61 m^2 g^{-1} (Table S2, Supporting Information), as well as to the optimization of the Cu–ZnO_x interface. The N_2O-RFC data reveal that the Cu dispersion in the CZA_r catalyst, when activated with the SC CO_2–EtOH mixture, is closely related to the treatment pressure. The dispersion follows the trend of 12 MPa (4 h) (12.95%) > 16 MPa (4 h) (10.40%) > CZA_r (10.08%) (Figure S13, Supporting

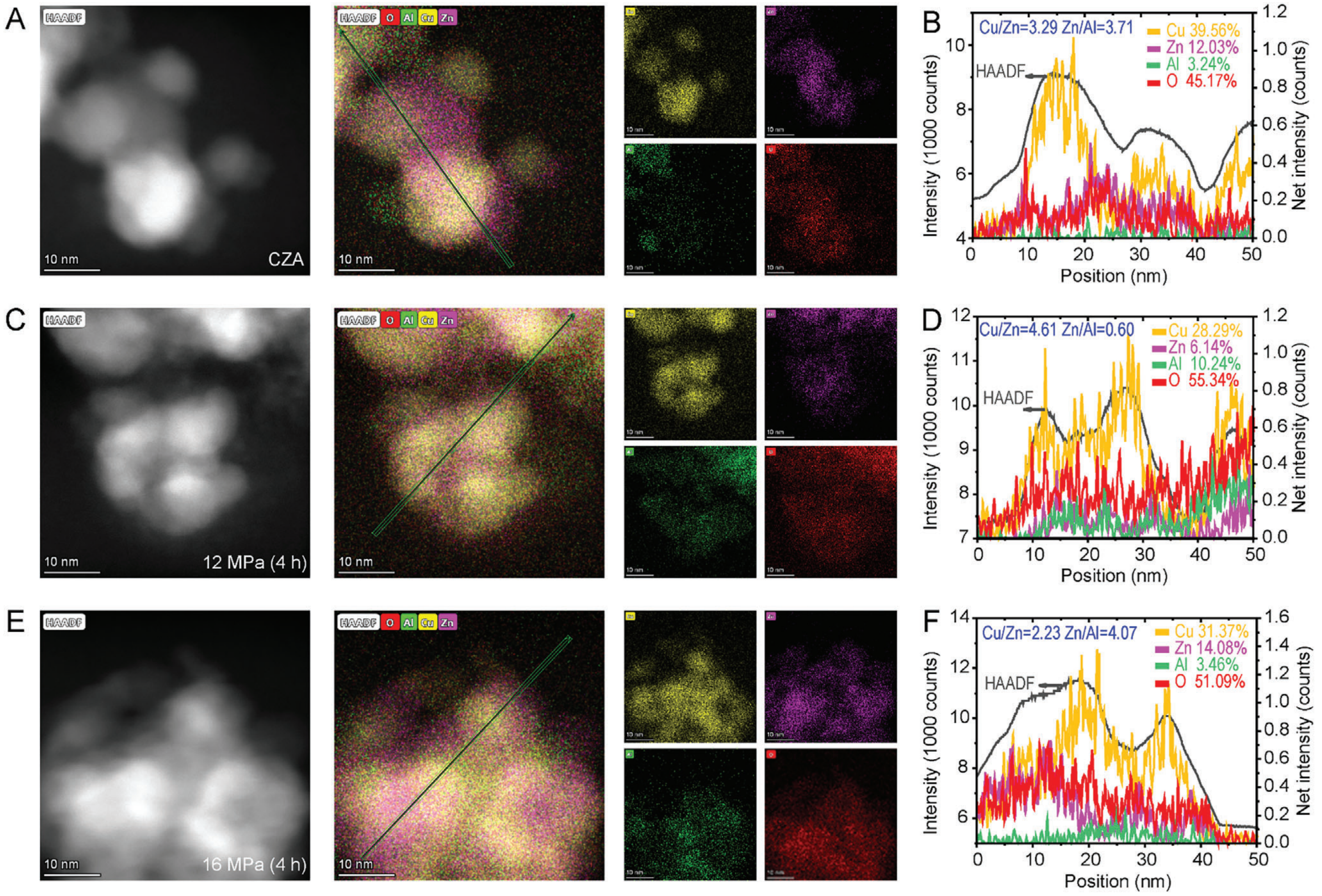

Figure 3. TEM characterization of the catalysts. A) HAADF STEM image and EDX elemental maps of CZA_r. Yellow: Cu; pink: Zn; green: Al; red: O. B) HAADF intensity and EDX line profiles along the green line in A). C,D) For the 12 MPa (4 h) sample. E,F) For the 16 MPa (4 h) sample.

Information). In addition, the enrichment of Al can be considered as being coupled to the formation of the new $Zn_xAl_2O_y$ phase. The beneficial role of structural reconstruction at the Cu–ZnO_x interface was further confirmed by the almost unchanged crystallite sizes and amorphous structure over the spent 12 MPa (4 h) catalyst, although the SMSI-induced partial coverage of the Cu surface with ZnO_x seems to have occurred again (Figure S14, Supporting Information). Recuperation and repeated processing in the SC CO_2–EtOH system were shown to facilitate these structural regenerations (Figure S15, Supporting Information).

2.3. Origin of the Active Sites

When CO_2 fluid is subjected to temperatures above its critical point of 31.1 °C and pressures exceeding 7.38 MPa, it enters a SC state known as a SC CO_2 fluid, in which chemical reactions and materials synthesis that cannot be achieved with traditional solvents can occur. To gain insights into the reactions in SC CO_2, one should first know that the critical characteristics of SC CO_2 are the inhomogeneity in space and the fluctuation in time.[22] When a solute is immersed in such an inhomogeneous medium, the average solvent density in the local region around a solute molecule will essentially differ from the bulk density, with typical increases/decreases of 50–300%. In addition, by adjusting the relevant parameters of the system, one can adjust the lifetime of the solvation structure and, consequently, the fluctuation of the polar environment (correlation time) around the solute molecule. In this context, SC CO_2 systems are being increasingly appreciated, especially very recently, for that the spatial inhomogeneity in the solvent density around reacting particles can dramatically affect the kinetics of diffusion-controlled reactions.[23]

We employed attenuated total reflectance infrared spectroscopy connected with a SC CO_2 apparatus to study the reaction kinetics dominated by fluctuation and to determine the origin of active sites in the SC CO_2–EtOH system. **Figure 4A** shows the time-dependent spectra of the fresh CZA_r subjected at 40 °C and 12 MPa. After the introduction of CO_2, a dynamic change in the adsorbates on the catalyst surface was observed. Ethoxy groups ($^*OC_2H_5$) bound at "bridging oxygen" vacancies (Zn–O_{br}–OC_2H_5) with strong, highly characteristic bands at 1043, 1377, 1450, and 2875–2970 cm^{-1} were identified as the main adsorbed species.[24] The peak intensity of Zn–OC_2H_5 (1119 cm^{-1}) on CZA_r, where the ethoxy groups are bound to the surface Zn atoms, is much weaker than that of Zn–O_{br}–OC_2H_5. The bands at 1273 and 1327 cm^{-1} can be assigned to the δ_{OH} and CH_2 wagging modes of a small number of ethanol molecules physisorbed on the surface. Note that surface-adsorbed $^*C_2H_5OH$

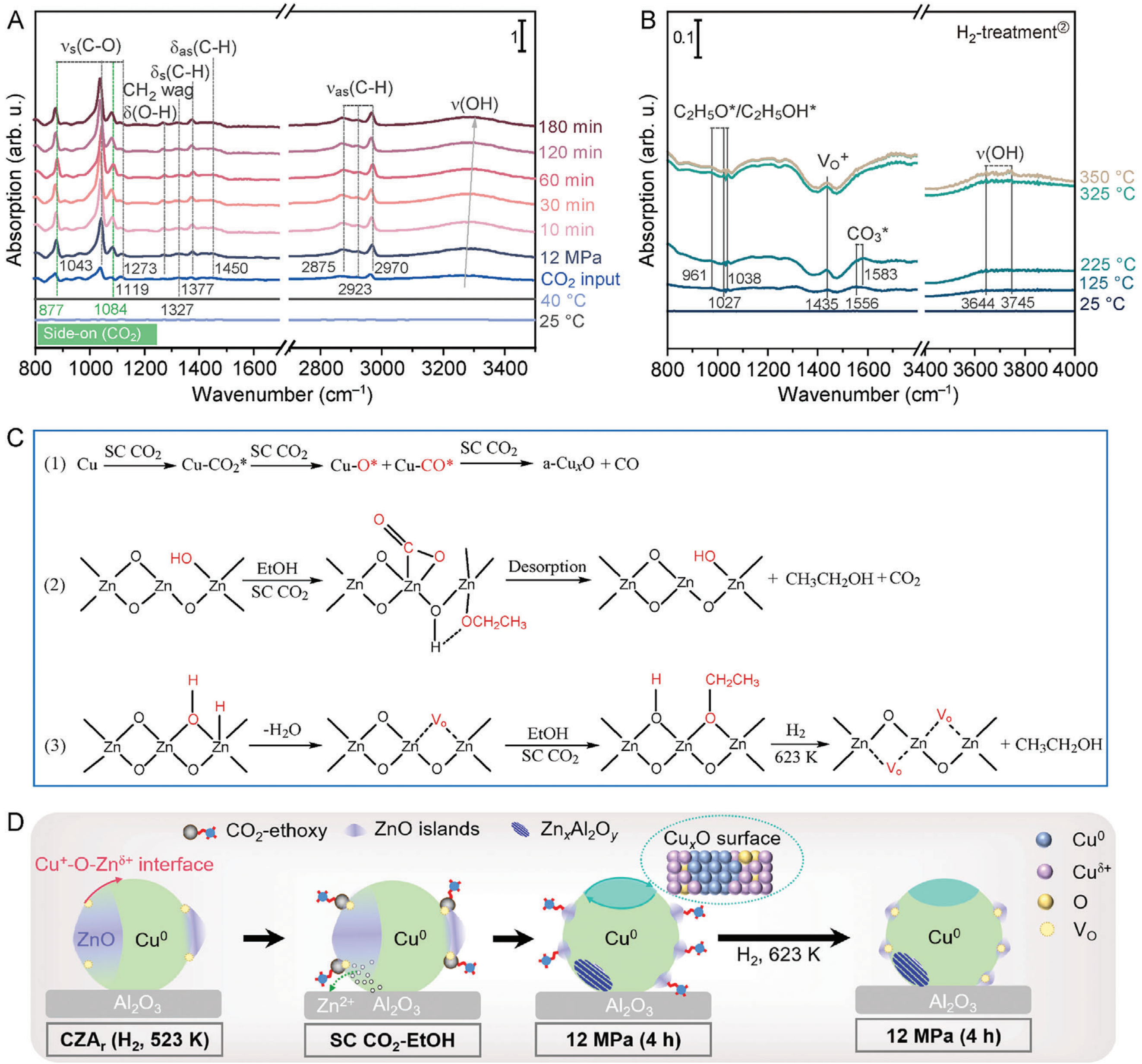

Figure 4. Structural evolution of the catalyst under the SC CO_2 environment. A) Time-dependent attenuated total reflectance infrared spectra of the fresh CZA_r in the SC CO_2–EtOH solvent system. B) In situ temperature-programmed DRIFTS of 12 MPa (4 h) with the spectra collected when the temperature was increased to 350 °C at a ramping rate of 5 °C min^{-1} in H_2. C) Proposed reaction mechanism for SC CO_2-induced activation. The illustrations show how the SC CO_2 and EtOH mixture critically affect the $Cu/ZnO/Al_2O_3$ structure. D) Schematic illustration of the structural reconstructions.

is believed to poison active sites and prevent the migration of oxide species.[10a,11] Notably, the migration and secondary uniform nucleation of ZnO_x on the Cu surface is realized in the fluctuating SC CO_2–EtOH medium. On the other hand, the broad bands at 3200–3400 cm^{-1} are derived from the intermolecular hydrogen bonds between CO_2 and ethanol, which can significantly promote the polarity and solubility parameters of SC CO_2.[25]

Meanwhile, the notable features of the C—O symmetric stretching modes at 877 and 1084 cm^{-1} suggest a η^2(C, O) structural motif of metal–CO_2 interactions, i.e., CO_2 being fixed in a "side-on" coordination manner.[26] The side-on bonded CO_2 is known to be unstable as it is a weakly bound van der Waals-type complex. The removal of CO_2 may thus occur during decompression. These observations suggest that the surface-adsorbed $^{*}OC_2H_5$ and CO_2 can act as the driving force for the migration of Zn species. The in situ diffuse reflectance infrared Fourier transform spectroscopy (DRIFTS) of the CZA_r and 12 MPa (4 h) catalysts after H_2 treatment reveals that the two samples have markedly different adsorption features (Figure 4B and Figure S16, Supporting Information). As the temperature was increased, adsorbed C_2H_5O/C_2H_5OH (961, 1027, and 1038 cm^{-1}),[27] water (3644 and 3745 cm^{-1}), and surface carbonate species (1556 and 1583 cm^{-1}) gradually appeared on the surface of the 12 MPa (4 h) catalyst.[28] The emergence of carbonate vibrational bands, correlating with residual CO_2 in the pipeline, underscores the high activity of ZnO_x nanoparticles towards CO_2 conversion. In particular, the band at 1435 cm^{-1} over the 12 MPa (4 h) catalyst that arises from $V_O{}^+$, where the oxygen vacancy (V_O) adsorbs a H_2 molecule and subsequently transfers electrons to it,[29] shows noticeable enhancement compared with the CZA_r catalyst. Meanwhile, the core level fitting of the O 1s signal also shows an increased presence of V_O on the surface of the 12 MPa (4 h) catalyst after H_2 treatment (Figure S17, Supporting Information). These results suggest that surface O_{br}–OC_2H_5 groups are removed as ethanol gas by protonation, thereby enabling the 12 MPa (4 h) catalyst with increased V_O.

It is worth summarizing the evidence for the participation of ethanol and CO_2 adsorbates on the catalyst in reconstructing the Cu surface, ZnO_x overlayer, and largely improved CO_2 hydrogenation reactivity (Figure 4C). For the Cu surface, the dissociation of CO_2 molecules generates *CO and *O species on the Cu surface. The subsequent penetration of *O inside the Cu lattice transforms metallic Cu^0 into an amorphous Cu_xO shell,[20] which generates a large number of Cu^0–Cu^+ surface sites. Based on the TEM and IR results in Figures 3 and 4, ethoxy groups and CO_2 molecules are responsible for the migration of Zn species, as discussed in other works.[24,30] We emphasize that ethanol species interact with Zn species in two different ways to reconstruct the ZnO_x overlayer. One is the Zn–OC_2H_5 species, which can readily be removed through combination with surface hydroxyl groups to desorb. The other is the O_{br}–OC_2H_5 species, which is bridge-bonded to two subsurface Zn cations and less active. Its removal occurs in the high-temperature range. On the other hand, the unreactive ethoxy groups can also be removed by protonation under reducing H_2 conditions, creating more V_O in the activated catalyst. Such optimization of the Cu–ZnO_x interface structure in the SC CO_2–EtOH solvent system can significantly increase the number of the Cu^0–O–$Zn^{\delta+}$ interface active sites. In addition, we hypothesize that the interaction of CO_2 with Zn species can induce the incorporation of Zn in the amorphous Al_2O_3 support and that the spinel-like structure of γ-Al_2O_3 can facilitate the formation of the new $Zn_xAl_2O_y$ phase.[31] An additional shoulder peak centered at 70 ppm (Al_{IV} site) in the ^{27}Al magic-angle spinning nuclear magnetic resonance and a simultaneous redshift in the Al_{VI} peak frequency strongly support our hypothesis (Figure S18, Supporting Information).[15a] This new phase helps to stabilize $Zn^{\delta+}$ species under the reaction conditions, thereby enhancing the catalytic activity of the Cu^0–O–$Zn^{\delta+}$ interface active sites. Based on the above results, we propose the mechanism for adsorbate (ethanol and SC CO_2 molecule)-induced activation and characteristics (Figure 4D). The behavior of the Cu/ZnO/Al_2O_3 surface depends on the reaction mixture and conditions, and the critical keys to high performance are the large accessible activated Cu_xO surface area and optimized Cu–ZnO_x interface.

2.4. Analysis of the Reaction Pathways

Temperature-programmed desorption (TPD) of CO_2, CO, H_2, and NH_3 experiments were carried out to examine the effect of the activated Cu_xO surface and optimized Cu–ZnO_x interface on the species adsorbed on the catalyst surface under the reaction conditions.

The CO_2-TPD results of all the catalysts confirm the presence of physically adsorbed CO_2 on hydroxyl groups ($\alpha < 150$ °C), chemically adsorbed CO_2 on the metal oxide ($200 < \beta < 500$ °C), and Cu–ZnO_x interfacial sites ($\gamma > 500$ °C) (**Figure 5A**).[32] Interestingly, the activated catalysts have distinct β and γ peaks compared with CZA_r, revealing a synchronous enhancement of surface and interface active sites. Particularly, an additional β peak at 255 °C on the 12 MPa (4 h) catalyst suggests a positive effect of the Cu_xO surface on the CO_2 adsorption. H_2-TPD data (Figure S19, Supporting Information) further demonstrate that the enhanced active sites endow the 12 MPa (4 h) catalyst with the strongest H_2 adsorption/activation capacity (0.558 mmol g^{-1}).[33] Meanwhile, the CO-TPD profile of the 12 MPa (4 h) catalyst exhibits a lower overall CO desorption and higher desorption temperature, revealing that SC CO_2 activation can efficiently adsorb and transform *CO intermediates (Figure 5B).[34] An increased acid site was also observed on the 12 MPa (4 h) catalyst (Figure 5C), which might be caused by the incorporation of Zn in γ-Al_2O_3.[35] Note that the changes in acid sites for the 12 MPa (4 h) catalyst are beneficial for high selectivity to CH_3OH even at a higher conversion rate. These findings demonstrate that exposing the CZA_r catalyst to the SC CO_2–EtOH mixture under reasonable pressure during activation can increase the number of the Cu^0–O–$Zn^{\delta+}$ interface sites owing to the secondary nucleation and growth of ZnO, as well as generate a massive number of the Cu^0–Cu^+ surface sites through the formation of a significantly accessible activated Cu_xO amorphous shell. In contrast, excessive treatment results in a thick ZnO_x overlayer, reducing the number of accessible Cu^0–Cu^+ surface sites on the surface of Cu_xO.

To date, the formate mechanism, where CO_2 binds through a C atom and a H atom coming from the dissociation of H_2 on metallic Cu^0, forming a bidentate formate (bi-HCOO*) intermediate on active ZnO sites, is most commonly identified as the reaction mechanism of CO_2 hydrogenation to CH_3OH.[4b] Another pathway involves CO generated from the RWGS reaction through HOCO* species. It is generally accepted for the hydrogenation of CO_2 on a Cu catalyst with inert support.[36] Analysis of the structural evolution under the SC CO_2 conditions and the catalytic performance over the activated catalysts have shown the favorable roles of the newly created Cu^0–Cu^+ surface sites and optimal Cu^0–O–$Zn^{\delta+}$ interface sites in CO_2 hydrogenation to CH_3OH. We thus hypothesize that both the formate (HCOO*) and CO-involved mechanisms act simultaneously over the activated catalyst during realistic conditions.

In situ temperature-programmed DRIFTS studies at atmospheric pressure were undertaken to gain further insight into the reaction pathway over the activated catalyst (170–250 °C). The catalysts were first reduced with a stream of H_2 at 350 °C for 1 h and then rinsed with Ar to remove weakly adsorbed molecules. Under the reaction conditions, the DRIFT spectra of the catalysts ($3H_2$:CO_2 treatment) show similar CO_3* species (Cu–CO_3* at 1269 and 1338 cm^{-1}, Zn–CO_3* at 1455–1513 cm^{-1}) and the adsorption of formate on Zn (bi-HCOO* at 1361 and 1589 cm^{-1}) with two O atoms bound to two adjacent Zn atoms (Figure 5D,E).[18] The peaks at 1026–1050 cm^{-1} can be assigned to the CH_3OH* and Zn–H_3CO* species. Overall, the generation

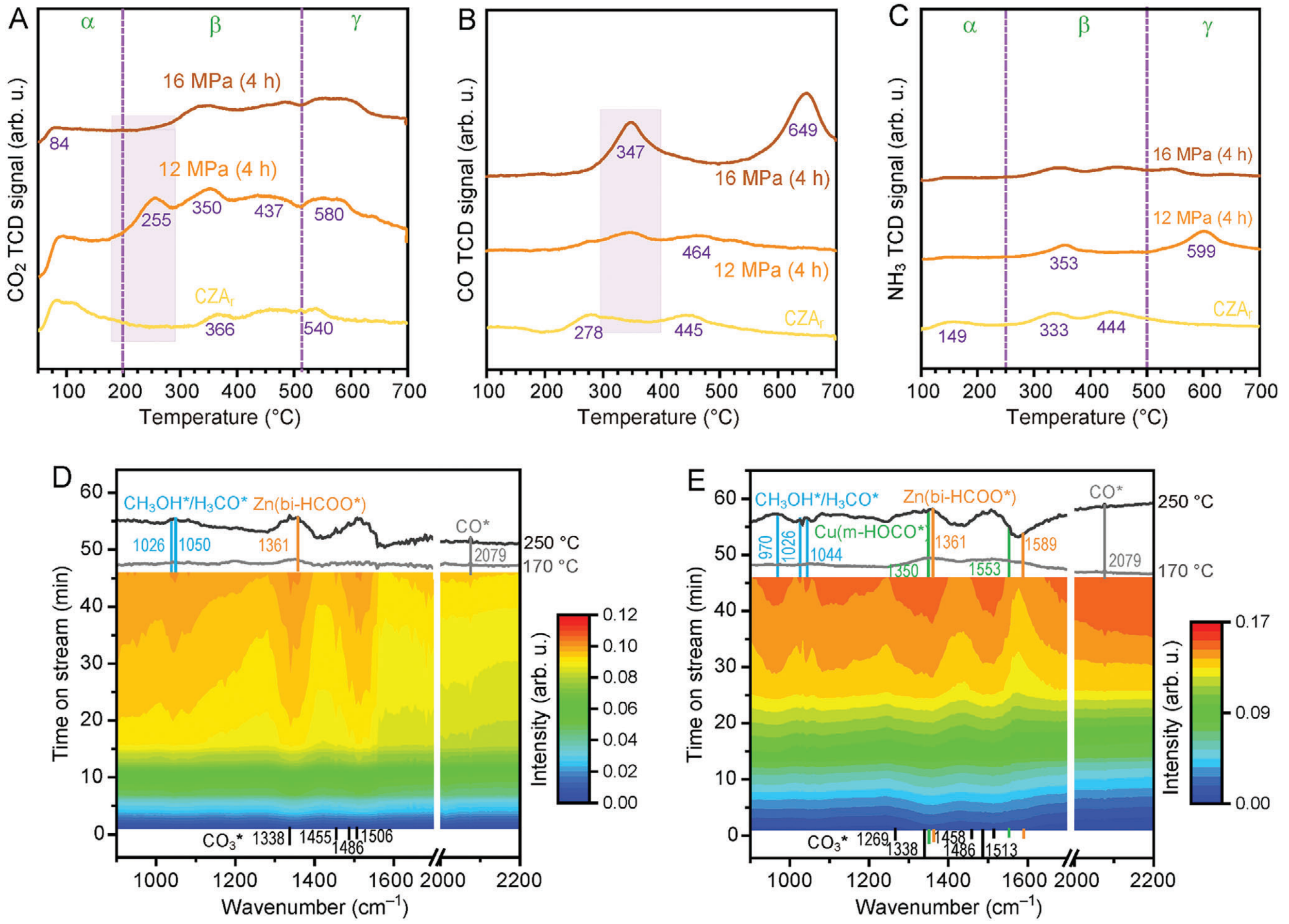

Figure 5. Identification of the active sites. A) CO_2-TPD, B) CO-TPD, and C) NH_3-TPD curves of the CZA$_r$, 12 MPa (4 h), and 16 MPa (4 h) catalysts. D, E) Time-dependent in situ DRIFTS spectra of the CZA$_r$ (D) and 12 MPa (4 h) (E) catalysts under feed gas with an H_2/CO_2 molar ratio of 3:1 from 170 to 210 °C under atmospheric pressure.

and consumption of Zn–HCOO* on the 12 MPa (4 h) catalyst were extremely fast compared to those of CZA$_r$, even at the very early stage (170 °C), demonstrating a highly reactive reaction on the activated catalyst. Furthermore, the single vibrational peak of Zn(bi-HCOO*) on CZA$_r$ suggests that the Cu^0–O–$Zn^{\delta+}$ interface site is the primary active site for CO_2 activation and conversion. Noticeably, except for the common formate species, adsorbed Cu–H_3CO* (970 cm^{-1}) and the formation of monodentate HOCO* species (m-HOCO* at 1350 and 1553 cm^{-1}) on Cu with the C atom bonded to the active Cu site appear on the activated catalyst.[37] As the temperature was increased, the conversion of m-HOCO* to H_3CO* species was much faster over bi-HCOO* on the 12 MPa (4 h) catalyst. More importantly, the DRIFT spectra of the activated catalyst show a twofold decrease in the integrated area of CO species (2079 cm^{-1}) compared to CZA$_r$, especially at a higher temperature (250 °C), indicating the efficient hydrogenation conversion of *CO intermediates on the 12 MPa (4 h) catalyst. The identification of Zn(bi-HCOO*) and Cu(m-HOCO*) intermediates and the decrease in the CO intensities, combined with the promotion of the reactivity of the activated catalyst, demonstrate that the exceptional reactivity induced by the SC CO_2–EtOH treatment is mediated by the dual-response pathway involving the formate and RWGS + CO hydrogenation mechanisms.

Accordingly, all components in the activated catalyst play important roles in the reaction. The involved components and roles can be summarized as follows. (i) The metallic Cu^0 sites at the surface and interface dominate the adsorption and activation of H_2. (ii) The small ZnO species that are uniformly distributed around the Cu particles help the dispersion of the Cu phase and stabilize the active Cu^+ sites at the surface of the Cu_xO amorphous shell or the Cu–ZnO_x interface. At the same time, the improved Cu–Zn synergy provides sufficient and stable Cu^0–O–$Zn^{\delta+}$ interface sites, which, together with the Cu^0–Cu^+ surface sites, activate CO_2 and initiate the subsequent hydrogenation steps by different mechanisms. (iii) The formation of $Zn_xAl_2O_y$ and the changes in acidic sites caused by the incorporation of Zn in the amorphous Al_2O_3 support promote the stability and selectivity of the activated catalyst. In addition, we conducted a comparative experiment using a Cu/ZnO/SiO_2 catalyst without Lewis acidic sites to further highlight the universality of the proposed supercritical CO_2 activation strategy (Figure S20, Supporting Information).[33,38] Similar phenomena of the amorphization of the Cu component as well as the secondary nucleation and

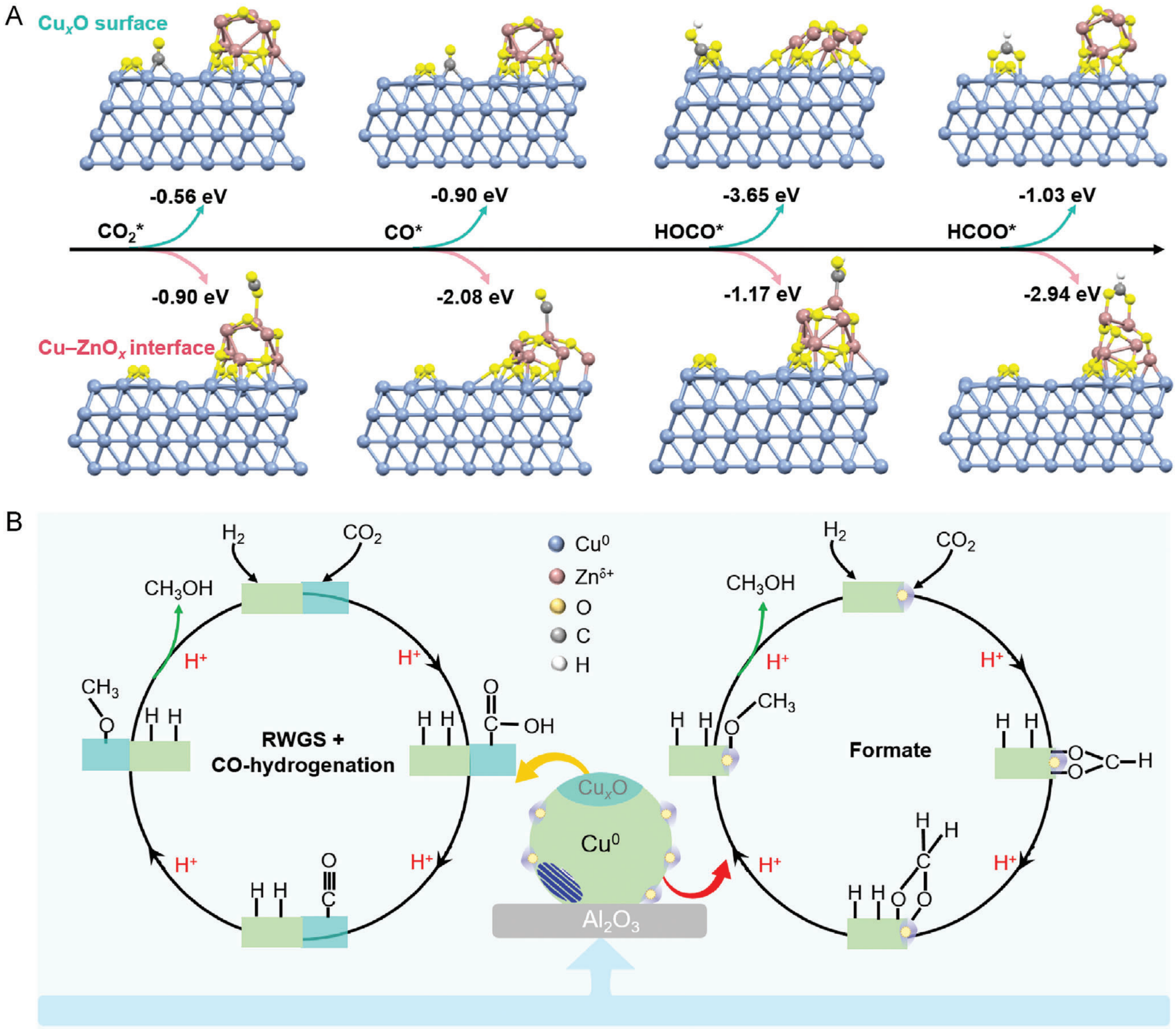

Figure 6. Analysis of the reaction pathway. A) DFT-optimized geometries of CO_2 and key intermediates adsorbed on the different sites of the activated catalyst and their adsorption energies, where the upper ones belong to Cu_xO and the bottom ones belong to Cu–ZnO_x on the 12 MPa (4 h) catalyst. Cu: blue; Zn: pink; O: yellow; C: grey; and H: white. B) Schematic diagram of the parallel reaction mechanisms on the Cu_xO surface and Cu–ZnO_x interface of the 12 MPa (4 h) catalyst for methanol synthesis from CO_2 hydrogenation.

growth of ZnO were observed in the activated Cu/ZnO/SiO_2 catalyst. As a result, the MeOH STY of the 12 MPa (4 h) Cu/ZnO/SiO_2 sample increased approximately by two folds, with a higher selectivity (42%), in comparison with its pristine counterpart at the reaction temperature of 250 °C.

Density functional theory (DFT) calculations provided additional fundamental insights into the MeOH reaction pathway over the activated catalyst. We note that even theoretically, it is challenging to elucidate such a promotion effect at the atomic level.[4b] We therefore proposed a simplified alternative solution, which is to calculate the adsorption energies of CO_2 and the key intermediates on the different sites. Cu nanoparticles were represented by a Cu(111) surface, which dominates on the X-ray diffraction patterns. The Cu_xO and Cu–ZnO_x sites under the reaction conditions were modeled using the optimized ZnO/Cu(111) structure, where a number of O atoms bind to Cu atoms on the surface (Figure S21, Supporting Information).

Figures 6A and S22 (Supporting Information) show the DFT-optimized geometries of CO_2 and the key intermediates adsorbed on the Cu_xO surface and Cu–ZnO_x interface, respectively. The corresponding adsorption energies on the different sites were calculated (Table S3, Supporting Information). We can see that the Cu_xO surface that arises from metallic Cu^0 allows the binding of CO_2 and CO, which can efficiently activate CO_2 and suppress CO desorption. Furthermore, the HOCO* adsorption energy over the Cu_xO surface is higher than that on the Cu–ZnO_x interface, indicating that the RWGS + CO hydrogenation route can be enhanced over the Cu_xO surface. In contrast, the preferential adsorption of the HCOO* intermediate at the Cu–ZnO_x interface facilitates formate hydrogenation. These results further support the hypothesis that both the surface Cu^0–Cu^+ sites and the interfacial Cu^0–O–$Zn^{\delta+}$ sites are active for MeOH synthesis from the CO_2–H_2 reaction, which involves different elementary reaction processes. Figure 6B illustrates the dual-response pathway of CO_2 hydrogenation to MeOH, where the Cu^0 site is responsible for H_2 activation, while the Cu^+ and $Zn^{\delta+}$ sites are proposed to promote not only CO_2 activation but also its further hydrogenation. The initial step of CO_2 hydrogenation on the Cu^0–O–$Zn^{\delta+}$ interface sites occurs through a formate mechanism, where CO_2 reacts with a surface H* to generate an adsorbed bi-HCOO* species. This bi-HCOO* species is then further hydrogenated, forming a H_2COO* species, which undergoes sequential hydrogenation at the Cu–ZnO_x interface to yield H_3CO* as the reactive intermediate for MeOH synthesis. The Cu–CO_3* species are easily desorbed to produce byproduct CO in this pathway. The parallel RWGS + CO hydrogenation mechanism occurs on the Cu^0–Cu^+ surface sites, which is preferred at higher reaction temperatures. The adsorbed CO_2 is hydrogenated to form an m-HOCO* species through Cu^+, followed by further hydrogenation that splits into CO* and H_2O. The further hydrogenation reaction of CO* gives a H_3CO* intermediate, with the final formation of CH_3OH. The synergistic effect of the Cu–ZnO_x interface and Cu_xO surface enables the Cu/ZnO/Al_2O_3 catalyst to be highly active, selective, and stable.

3. Conclusion

In summary, we have presented a supercritical CO_2 activation strategy that synchronously perfects the SMSI-induced Cu^0–O–$Zn^{\delta+}$ interface and exposed Cu^0–Cu^+ surface sites by manipulating the adsorbate diffusion kinetics. Adsorbed *OC_2H_5 and CO_2 species on ZnO_x have been demonstrated to effectively homogenize the secondary nucleation sites of ZnO_x on the Cu surface and cause the incorporation of Zn in the Al_2O_3 support. Further removal of *OC_2H_5 creates more V_O in the activated catalyst, and the formation of the $Zn_xAl_2O_y$ spinel phase contributes to the improved stability of $Zn^{\delta+}$ species under the reaction conditions. Moreover, CO_2 adsorption on exposed metallic Cu^0 results in the formation of an activated Cu_xO amorphous shell. Such a structural evolution, including an enlarged accessible Cu_xO surface and optimized Cu–ZnO_x interface, unlocks the dual-response pathway in methanol synthesis. CO_2 preferentially adsorbs on the Cu_xO surface in a monodentate bonding mode and undergoes hydrogenation through the reverse water-gas shift plus CO hydrogenation pathway. At the same time, the formate pathway occurs on the Cu–ZnO_x interface. The opportunities offered by our strategy to design active surface and interface sites at the atomic scale open new avenues for improving the reactivity of supported metal catalysts.

Supporting Information

Supporting Information is available from the Wiley Online Library or from the author.

Acknowledgements

This work was partially supported by the National Natural Science Foundation of China (22305091, 21903070), the Natural Science Foundation of Henan Province (232300420144), the Key Research Program of Higher Education Institutions in Henan Province (24A150020), and the Key Technology Research and Development Program of Henan (232102230014). The schematic of the SC CO_2–EtOH system in the Table of Contents image was modified from Servier Medical Art (http://smart.servier.com/), which is licensed under a Creative Common Attribution 3.0 Generic License (https://creativecommons.org/licenses/by/3.0/).

Conflict of Interest

The authors declare no conflict of interest.

Author Contributions

Y.N.Z., S.R.Z., and J.F.W. conceived the project. Y.N.Z., J.Y.J., S.R.Z., and J.F.W. supervised the project. Y.N.Z., Y.S.W., and R.J.L. performed the experiments, collected, and analyzed the data. Y.N.Z. and J.F.W. drafted the manuscript and figures, and all authors revised them.

Data Availability Statement

The data that support the findings of this study are available from the corresponding author upon reasonable request.

Keywords

dual-response pathway, methanol synthesis, strong metal–support interaction, supercritical CO_2 activation, ternary Cu/ZnO/Al_2O_3 catalyst

Received: January 9, 2025
Revised: February 8, 2025

---

[1] a) S. Kar, R. Sen, A. Goeppert, G. K. S. Prakash, *J. Am. Chem. Soc.* **2018**, *140*, 1580; b) S. Navarro-Jaén, M. Virginie, J. Bonin, M. Robert, R. Wojcieszak, A. Y. Khodakov, *Nat. Rev. Chem.* **2021**, *5*, 564.
[2] A. Beck, M. A. Newton, L. G. A. van de Water, J. A. van Bokhoven, *Chem. Rev.* **2024**, *124*, 4543.
[3] C. R. International, https://www.carbonrecycling.is, **2024**.
[4] a) M. Zabilskiy, V. L. Sushkevich, D. Palagin, M. A. Newton, F. Krumeich, J. A. van Bokhoven, *Nat. Commun.* **2020**, *11*, 2409; b) G. Pacchioni, *ACS Catal.* **2024**, *14*, 2730.
[5] a) M. Xu, M. Peng, H. Tang, W. Zhou, B. Qiao, D. Ma, *J. Am. Chem. Soc.* **2024**, *146*, 2290; b) T. Pu, W. Zhang, M. Zhu, *Angew. Chem., Int. Ed.* **2023**, *62*, e202212278.
[6] a) J. Dong, Q. Fu, H. Li, J. Xiao, B. Yang, B. Zhang, Y. Bai, T. Song, R. Zhang, L. Gao, J. Cai, H. Zhang, Z. Liu, X. Bao, *J. Am. Chem. Soc.* **2020**, *142*, 17167; b) H. Xin, L. Lin, R. Li, D. Li, T. Song, R. Mu, Q. Fu, X. Bao, *J. Am. Chem. Soc.* **2022**, *144*, 4874; c) L. Cai, S. Han, W. Xu, S. Chen, X. Shi, J. Lu, *Angew. Chem., Int. Ed.* **2024**, *63*, e202404398.
[7] a) T. Song, R. Li, J. Wang, C. Dong, X. Feng, Y. Ning, R. Mu, Q. Fu, *Angew. Chem., Int. Ed.* **2024**, *63*, e202316888; b) J. C. Matsubu, S. Zhang, L. DeRita, N. S. Marinkovic, J. G. Chen, G. W. Graham, X. Pan, P. Christopher, *Nat. Chem.* **2017**, *9*, 120.
[8] a) T. Lunkenbein, F. Girgsdies, T. Kandemir, N. Thomas, M. Behrens, R. Schlögl, E. Frei, *Angew. Chem., Int. Ed.* **2016**, *55*, 12708; b) N.

J. Divins, D. Kordus, J. Timoshenko, I. Sinev, I. Zegkinoglou, A. Bergmann, S. W. Chee, S. Widrinna, O. Karslıoğlu, H. Mistry, M. L. Luna, J. Q. Zhong, A. S. Hoffman, A. Boubnov, J. A. Boscoboinik, M. Heggen, R. E. Dunin-Borkowski, S. R. Bare, B. R. Cuenya, *Nat. Commun.* **2021**, *12*, 1435.

[9] a) N. Ortner, D. Zhao, H. Mena, J. Weiß, H. Lund, S. Bartling, S. Wohlrab, U. Armbruster, E. V. Kondratenko, *ACS Catal.* **2023**, *13*, 60; b) B. Liang, J. Ma, X. Su, C. Yang, H. Duan, H. Zhou, S. Deng, L. Li, Y. Huang, *Ind. Eng. Chem. Res.* **2019**, *58*, 9030.

[10] a) F. Polo-Garzon, T. F. Blum, V. Fung, Z. Bao, H. Chen, Z. Huang, S. M. Mahurin, S. Dai, M. Chi, Z. Wu, *ACS Catal.* **2020**, *10*, 8515; b) F. Polo-Garzon, T. F. Blum, Z. Bao, K. Wang, V. Fung, Z. Huang, E. E. Bickel, D.-e. Jiang, M. Chi, Z. Wu, *ACS Catal.* **2021**, *11*, 1938; c) D. Li, F. Xu, X. Tang, S. Dai, T. Pu, X. Liu, P. Tian, F. Xuan, Z. Xu, I. E. Wachs, M. Zhu, *Nat. Catal.* **2022**, *5*, 99; d) Y. F. Shi, P. L. Kang, C. Shang, Z. P. Liu, *J. Am. Chem. Soc.* **2022**, *144*, 13401.

[11] S. Jin, Z. Zhang, D. Li, Y. Wang, C. Lian, M. Zhu, *Angew. Chem., Int. Ed.* **2023**, *135*, e202301563.

[12] a) Y. Zhou, P. Yan, S. Zhang, C. Ma, T. Ge, X. Zheng, L. Zhang, J. Jiang, Y. Shen, J. Chen, Q. Xu, *Nano Today* **2021**, *40*, 101272; b) Y. Zhou, Q. Xu, T. Ge, X. Zheng, L. Zhang, P. Yan, *Angew. Chem., Int. Ed.* **2020**, *59*, 3322; c) T. Ge, W. Cui, Q. Xu, *Angew. Chem., Int. Ed.* **2023**, *135*, e202300446.

[13] S. Kuld, C. Conradsen, P. G. Moses, I. Chorkendorff, J. Sehested, *Angew. Chem., Int. Ed.* **2014**, *53*, 5941.

[14] M. B. Fichtl, D. Schlereth, N. Jacobsen, I. Kasatkin, J. Schumann, M. Behrens, R. Schlögl, O. Hinrichsen, *Appl. Catal. A: Gen.* **2015**, *502*, 262.

[15] a) M. Nadjafi, A. M. Kierzkowska, A. Armutlulu, R. Verel, A. Fedorov, P. M. Abdala, C. R. Müller, *J. Phys. Chem. C* **2021**, *125*, 14065; b) X. Huang, A. Beck, A. Fedorov, H. Frey, B. Zhang, B. Klötzer, J. A. van Bokhoven, C. Copéret, M. G. Willinger, *ChemCatChem* **2022**, *14*, 202201280.

[16] X. Zhang, G. Zhang, W. Liu, F. Yuan, J. Wang, J. Zhu, X. Jiang, A. Zhang, F. Ding, C. Song, X. Guo, *Appl. Catal. B: Environ* **2021**, *284*, 119700.

[17] H. Nguyen-Phu, E. W. Shin, *J. Catal.* **2019**, *373*, 147.

[18] B. Xie, R. J. Wong, T. H. Tan, M. Higham, E. K. Gibson, D. Decarolis, J. Callison, K. F. Aguey-Zinsou, M. Bowker, C. R. A. Catlow, J. Scott, R. Amal, *Nat. Commun.* **2020**, *11*, 1615.

[19] C. J. Powell, *J. Electron Spectrosc. Relat. Phenom.* **2012**, *185*, 1.

[20] C. Chen, X. Yan, Y. Wu, X. Zhang, S. Liu, F. Zhang, X. Sun, Q. Zhu, L. Zheng, J. Zhang, X. Xing, Z. Wu, B. Han, *Nat. Commun.* **2023**, *14*, 1092.

[21] J. Zhu, D. Ciolca, L. Liu, A. Parastaev, N. Kosinov, E. J. M. Hensen, *ACS Catal.* **2021**, *11*, 4880.

[22] O. Kajimoto, *Chem. Rev.* **1999**, *99*, 355.

[23] a) D. Zhang, L. Zhang, S. Zhang, X. Guo, B. Yang, Y. Zhou, *J. CO2 Util.* **2024**, *80*, 102694; b) Y. Zhou, P. Yan, S. Zhang, Y. Zhang, H. Chang, X. Zheng, J. Jiang, Q. Xu, *Fundam. Res.* **2021**, *2*, 674; c) Y. Zhou, Q. Xu, *Phys. Chem. Chem. Phys.* **2023**, *25*, 3607.

[24] a) G. A. M. Hussein, N. Sheppard, M. I. Zaki, R. B. Fahim, *J. Chem. Soc.* **1991**, *87*, 2661; b) J. Zhang, C. Shang, Z. An, Y. Zhu, H. Song, Z. Chai, X. Shu, L. Zheng, J. He, *Angew. Chem., Int. Ed.* **2023**, *62*, e202312068.

[25] P. Lalanne, T. Tassaing, Y. Danten, F. Cansell, S. Tucker, M. Besnard, *J. Phys. Chem. A* **2004**, *108*, 2617.

[26] a) J. Mascetti, M. Tranquille, *J. Phys. Chem.* **1988**, *92*, 2177; b) L. G. Dodson, M. C. Thompson, J. M. Weber, *Annu. Rev. Phys. Chem.* **2018**, *69*, 231.

[27] L. Zhang, J. Feng, L. Wu, X. Ma, X. Song, S. Jia, X. Tan, X. Jin, Q. Zhu, X. Kang, *J. Am. Chem. Soc.* **2023**, *145*, 21945.

[28] M. Li, Z. Wu, S. Overbury, *J. Catal.* **2013**, *306*, 164.

[29] Z. Wang, K. Wang, H. Wang, X. Chen, W. Dai, X. Fu, *Catal. Sci. Technol.* **2018**, *8*, 3260.

[30] a) L. Gamble, L. S. Jung, C. T. Campbell, *Surf. Sci.* **1996**, *348*, 1; b) G. Kwak, K. Yong, *J. Phys. Chem. C* **2008**, *112*, 3036.

[31] H. Zhou, Y. Ji, Y. Wang, K. Feng, B. Luan, X. Zhang, L. Q. Chen, *Acta Mater.* **2024**, *263*, 119513.

[32] S. Wang, L. Zhang, W. Zhang, P. Wang, Z. Qin, W. Yan, M. Dong, J. Li, J. Wang, L. He, *Chem* **2020**, *6*, 3344.

[33] Y. Wang, X. Wang, Z. Yan, C. Xu, W. Zhang, H. Ban, C. Li, *J. Catal.* **2022**, *412*, 10.

[34] K. Wang, H. Qin, J. Li, Q. Cheng, Y. Zhu, H. Hu, J. Peng, S. Chen, G. Wang, S. Chou, *Appl. Catal. B: Environ.* **2023**, *332*, 122763.

[35] a) J. Trawczyński, A. Kubacki, J. Wrzyszcz, M. Zawadzki, H. Grabowska, W. Miśta, *React. Kinet. Catal. Lett.* **2002**, *76*, 259; b) S. Wu, W. Sun, J. Chen, J. Zhao, Q. Cao, W. Fang, Q. Zhao, *J. Catal.* **2019**, *377*, 110.

[36] S. Kattel, P. J. Ramírez, J. G. Chen, J. A. Rodriguez, P. Liu, *Science* **2017**, *355*, 1296.

[37] M. Yang, J. Yu, A. Zimina, B. B. Sarma, J. D. Grunwaldt, H. Zada, L. Wang, J. Sun, *Angew. Chem., Int. Ed.* **2024**, *63*, e202312292.

[38] E. Lam, J. J. Corral-Pérez, K. Larmier, G. Noh, P. Wolf, A. Comas-Vives, A. Urakawa, C. Copéret, *Angew. Chem., Int. Ed.* **2019**, *58*, 13989.